



# Topological-cavity surface-emitting laser

Lechen Yang<sup>1,2,4</sup>, Guangrui Li<sup>1,4</sup>, Xiaomei Gao<sup>1</sup> and Ling Lu<sup>1,3</sup>

**Output power and beam quality are the two main bottlenecks for semiconductor lasers—the favourite light sources in countless applications because of their compactness, high efficiency and cheapness. Both limitations are due to the fact that it becomes increasingly harder to stabilize a single-mode laser over a broader chip area without multi-mode operations. Here we address this fundamental difficulty with the Dirac-vortex topological cavity<sup>1</sup>, which offers the optimal single-mode selection in two dimensions. Our topological-cavity surface-emitting laser (TCSEL) exhibits 10 W peak power, sub-1° divergence angle and 60 dB side-mode suppression, among the best-reported performance ever at 1,550 nm—the most important telecommunication and eye-safe wavelength where high-performance surface emitters have always been difficult to make<sup>2</sup>. We also demonstrate the multi-wavelength capability of two-dimensional TCSEL arrays that are not generally available for commercial lasers<sup>2,3</sup>. TCSEL, as a new-generation high-brightness surface emitter, can be directly extended to any other wavelength range and is promising for an extremely wide variety of uses.**

Topological physics<sup>4,5</sup> has been the focus of fundamental research since the discovery of the quantum Hall effect, revealing that real-world physical quantities can literally remain invariant under continuous variations of system parameters. Although such robust phenomena can, in principle, dramatically improve the stability and specifications of practical devices, the applications of topological physics remain elusive. Surprisingly, it was pointed out<sup>1</sup> that conventional diode-laser products already contain key grating elements that are mathematically equivalent to one-dimensional (1D) topological models. Figure 1 shows the distributed feedback (DFB)<sup>6</sup> laser powering Internet communications as well as the vertical-cavity surface-emitting laser (VCSEL)<sup>7</sup> enabling cell-phone facial recognition; both of them adopt the mid-gap topological mode in their optimized resonator designs. Meanwhile, a more advanced topological resonator has been proposed in two dimensions for the purist single-mode spectrum over the broadest area, known as the Dirac-vortex cavity<sup>1</sup>. In this work, we demonstrate the Dirac-vortex topological-cavity surface-emitting laser (TCSEL), with outstanding performance at 1,550 nm, under optical pumping and at room temperature.

Compared with standard industrial products of DFB<sup>3</sup> and VCSEL<sup>2</sup> (Fig. 1), TCSEL surpasses with regard to both power and divergence angle by orders of magnitudes, as well as offers the new feature of monolithic multi-wavelength surface-emitting arrays. Comparing the pioneering photonic-crystal surface-emitting laser (PCSEL) with similar performance<sup>7–9</sup> or similar wavelength<sup>10–13</sup>, TCSEL has a stabler mechanism (mid-gap versus band-edge modes) for single-mode operation (Supplementary Fig. s1). In distinction to the latest works on topological lasers<sup>14–19</sup>, TCSEL

outperforms its commercial counterparts. TCSEL employs a two-dimensional (2D) broad-area mid-gap defect mode, whose design is consistent with the historical success and development of semiconductor lasers (DFB, VCSEL and PCSEL): from one to two dimensions, from the band-edge to mid-gap mode and from edge emitter to surface emitter<sup>1</sup>.

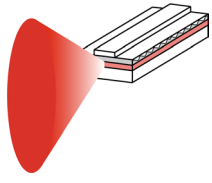
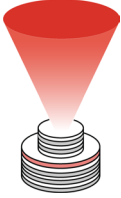
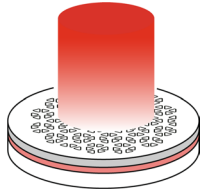
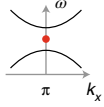
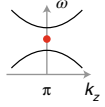
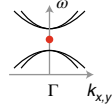
A TCSEL can be viewed as the 2D upgrade of the 1D phase-shifted DFB laser (Fig. 1), with a second-order grating for vertical emission. A schematic of our TCSEL is shown in Fig. 2a, where the topological cavity is formed by placing an amorphous silicon (a-Si) photonic-crystal layer (320 nm, refractive index  $n = 3.4$ ) on a waveguide layer (225 nm,  $n = 3.4$ ) containing multiple quantum wells (MQWs) on the InP ( $n = 3.1$ ) substrate. The photonic crystal layer, with the Dirac-vortex pattern, is chosen to have enough modal overlap (coupling strength) so that the MQWs do not need to be etched to maintain the best material quality of the active region. The vertical epitaxy structure and the corresponding confinement factors are given in Supplementary Fig. s2. The Dirac-vortex pattern has a honeycomb air-hole lattice with a generalized Kekulé modulation on each supercell (Fig. 2b). Within each supercell, one sub-lattice (three triangles) is shifted away from its original position with modulation amplitude  $m$  and correlated phase  $\varphi$ . To generate a  $2\pi$  vortex bandgap, the supercell with continuous phase variation from 0 to  $2\pi$  is angularly arranged around the cavity centre.

The modulation amplitude (sub-lattice shift)  $m$  is the key parameter of the TCSEL studied in this paper. Increasing  $m$  enlarges the Dirac-gap size and shrinks the modal area of the mid-gap mode. A larger  $m$  also enhances the out-of-plane emission, due to the increasing coupling strength of the second-order grating. Other parameters of the Dirac-vortex cavity (discussed elsewhere<sup>1</sup>) are left for further optimization. For example, the vortex radius ( $R$ ) is zero in this work, which is chosen to simplify the design and guarantee a single mode inside the bandgap (Supplementary Fig. s3).

It is not computationally feasible to model the entire TCSEL with full-wave simulations, whose device size is thousands of periods of non-periodic lattices in a three-dimensional waveguide. We adopt the quasi-analytical coupled wave theory that has been the standard approach to model DFB lasers<sup>20</sup> and PCSELs<sup>21</sup>. We extend this method to model a TCSEL by introducing spatially non-uniform coupling coefficients (Methods). The supercell band structures are plotted in Fig. 2c for the unperturbed supercell of  $m = 0$  and for the modulated supercell of  $m = 0.2a$  and  $\varphi = 2\pi/3$ . The fourfold Dirac point opens for all the values of  $\varphi$  with non-zero  $m$ .

The eigenmode solutions of a typical TCSEL (diameter, 500  $\mu\text{m}$ ) are shown in Fig. 2d. The red circle—of the lowest threshold gain—is the topological mid-gap mode that lases first. The blue circles are the continuum modes originating from the bulk bands. Although one bulk dispersion bends across the bandgap along the  $\Gamma$ –M direction (Fig. 2c), it has little effect on the topological mode (Supplementary

<sup>1</sup>Institute of Physics, Chinese Academy of Sciences/Beijing National Laboratory for Condensed Matter Physics, Beijing, China. <sup>2</sup>School of Physical Sciences, University of the Chinese Academy of Sciences, Beijing, China. <sup>3</sup>Songshan Lake Materials Laboratory, Dongguan, China. <sup>4</sup>These authors contributed equally: Lechen Yang, Guangrui Li. ✉e-mail: [linglu@iphy.ac.cn](mailto:linglu@iphy.ac.cn)

	Edge emitter		Surface emitter	
	DFB (phase shift)	VCSEL (Bragg mirror)	TCSEL (Dirac vortex)	
Device schematic				
Area	~300.0 $\mu\text{m} \times 1.5 \mu\text{m}$	~5 $\mu\text{m} \times 5 \mu\text{m}$	>500 $\mu\text{m} \times 500 \mu\text{m}$	
Power	~mW	~mW	~W	
Divergence	~20° $\times$ 40°	~20° $\times$ 20°	<1° $\times$ 1°	
Lasing mode	Single mode	Doubly degenerate	Single mode	
Topological mid-gap mode				
	Standard commercial products		This work	

**Fig. 1 | Single-mode lasers of topological mid-gap modes.** In one dimension, a DFB laser with phase shift as well as VCSEL lase at the mid-gap mode (red dot). In two dimensions, the TCSEL enables broad-area single-mode operation, offering much higher surface-emitting power and much narrower beam angle compared with its 1D counterparts. Here  $\omega$  is the frequency and  $k_{x,y,z}$  are the wavevectors.

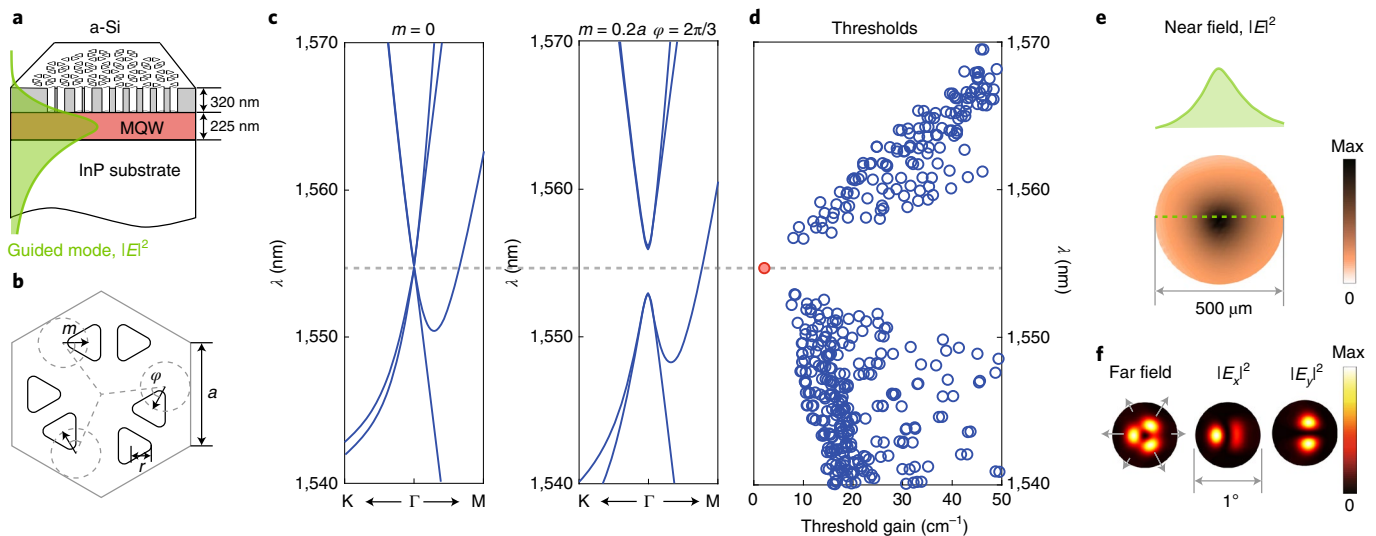


**Fig. 2 | TCSEL modelled by the coupled wave theory.** **a**, TCSEL structure with the vertical-mode profile in green. The refractive indices of the layers are  $n_{\text{a-Si}} = 3.4$ ,  $n_{\text{MQW}} = 3.4$  and  $n_{\text{InP}} = 3.1$ . **b**, Generalized Kekulé modulation of the honeycomb supercell. **c**, Band structure of the TE-like modes of the unperturbed supercell  $m = 0$  and perturbed supercell  $m = 0.2a$ ,  $\varphi = 2\pi/3$ . **d**, Eigenmode thresholds of TCSEL with air-hole filling ratio  $r/a = 0.32$  and cavity diameter of 500  $\mu\text{m}$ . The red circle indicates the topological mid-gap mode. **e**, Near field of the topological mode. **f**, Far fields of different polarization directions.

Fig. s4). The fact that the defect mode is well separated from the continuum modes ensures the stable single-mode lasing by maximizing the free spectral range and threshold gain difference with the rest modes. In the case of PCSEL, the band-edge lasing mode is at the end of the closely spaced continuum bulk modes, resulting in less stabler single-mode operations with much smaller free spectral range and threshold gain difference (compared in Supplementary Fig. s1). The near field (Fig. 2e) is a defect mode peaking at the cavity centre and decaying into the cladding. The far field (Fig. 2f) is a donut beam with three main lobes. If we keep increasing the

device size beyond 500  $\mu\text{m}$  by adding more photonic-crystal periods, the far field turns into a ring and the divergence angle narrows (Supplementary Fig. s5). Both near and far fields have the same  $C_{3v}$  symmetry as that of the Dirac-vortex cavity<sup>1</sup>. The mode profiles of the other competing modes are plotted in Supplementary Fig. s6.

Our TCSEL fabrication includes the deposition of a-Si on the MQW epi-structure by chemical vapour deposition and patterning of the a-Si layer by electron-beam lithography (EBL) and dry etching (Methods and Supplementary Fig. s7). The vortex structure of TCSEL can be clearly seen in the optical microscopy and scanning

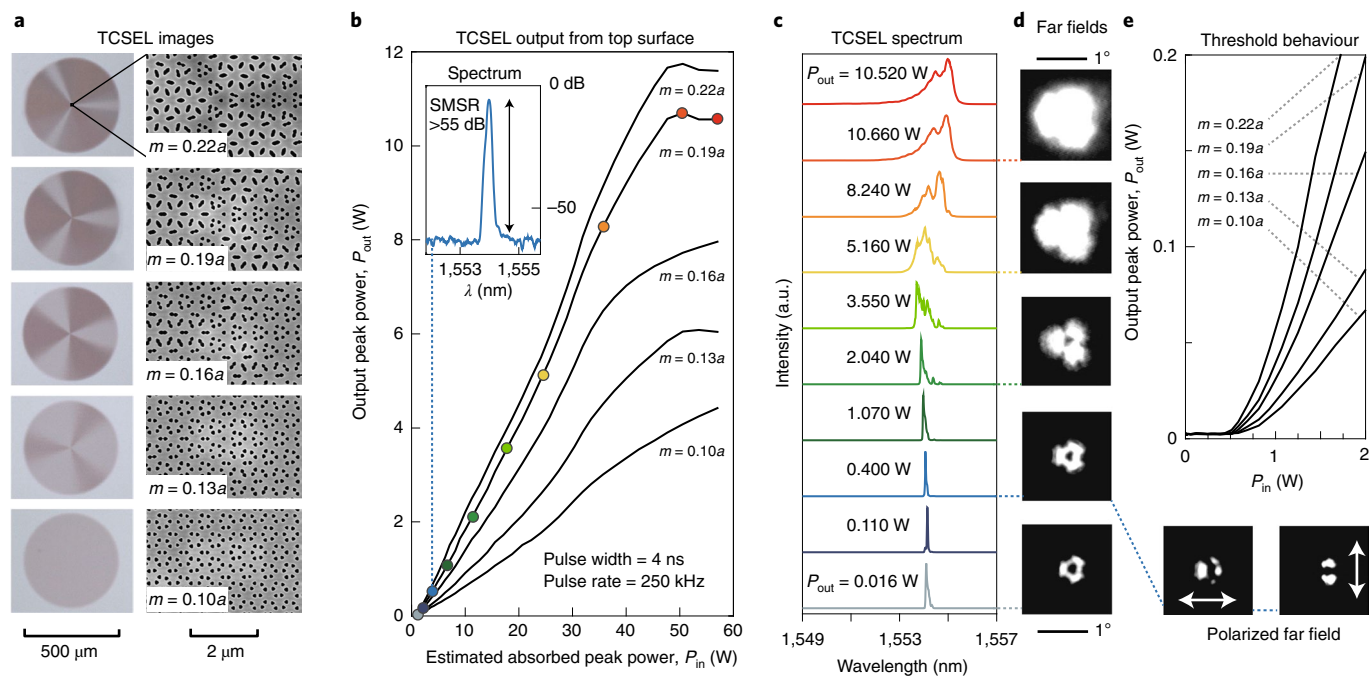


**Fig. 3 | TCSEL performance.** **a**, Optical microscopy and scanning electron microscopy images of TCSELs. **b**, Light-in and light-out curves of TCSELs with different modulation amplitudes  $m$ . The inset shows the data for SMSR greater than 55 dB and linewidth less than 0.03 nm. **c**, Lasing spectra of the linear scale with  $m = 0.19a$  at different output powers, taken using the finest OSA resolution of 0.01 nm. **d**, Evolution of the far field at different pumping conditions. **e**, Threshold behaviours of the data in **b**. Similar device performances are obtained from five independent fabrication runs.

electron microscopy images (Fig. 3a), where the lattice constant  $a = 325$  nm and air-hole size  $r/a = 0.32$ .

To test the high-power characteristics of TCSEL with minimal heating effects at room temperature, these devices are optically pumped under pulsed condition by a 1,064 nm fibre laser. The lasing spectrum is measured using an optical spectrum analyser (OSA). The power is collected by a power meter in the far field, and the far-field pattern is imaged by an infrared camera. More testing details are provided in Methods and Supplementary Fig. s8. We emphasize that the pulse conditions used in this work (4 ns duration and 250 kHz repetition rate corresponding to 0.1% duty cycle) are suitable for light detection and ranging (LiDAR) applications using the direct time-of-flight method.

We would like to explore the largest device size because for single-mode lasers, the larger the area, the higher the power and lower the beam divergence angle. Therefore, we set the device size to be 500  $\mu\text{m}$ —the limit of our EBL window—and tune the modulation amplitude  $m$  to maximize the surface-emitting power. In Fig. 3b, the light-in and light-out curves show a continuing increase of slope with  $m$ , ranging from  $0.10a$  to  $0.22a$ . If the sub-lattice shift ( $m$ ) increases further, the neighbouring air holes merge together and the slope efficiency drops eventually. In Supplementary Fig. s9, we also vary the device size from 200 to 500  $\mu\text{m}$  for fixed  $m = 0.19a$  to confirm that we reach the best performance from the current size constraint of fabrication.

Here 10 W, a remarkably high peak power at 1,550 nm, is collected in the far field from the top surface of the TCSEL (Fig. 3b). In comparison, a commercial 1,550 nm DFB typically outputs tens of milliwatts<sup>3</sup> and a VCSEL outputs a few milliwatts of power<sup>2</sup>. Biased more than 100 times above the threshold, the TCSEL output eventually saturates above 10 W, known as thermal rollover. The common reasons for this power-level saturation are carrier escaping the active region and an increase in the non-radiative recombination rate with temperature. At the highest pumping

levels in Fig. 3c, the lasing spectrum redshifts as the refractive index increases with temperature<sup>22</sup>. The zoomed-in threshold behaviour is shown in Fig. 3e and Supplementary Fig. s10, and the linewidth-narrowing data are presented in Supplementary Fig. s11. We numerically estimate that about 20% of the incident 1,064 nm pump power is absorbed by the MQW layer. Consequently, the slope efficiency is around 25% for these TCSELs. We emphasize that throughout this paper, we do not include the power emitted from the bottom surface, which is about half the top-emitting power measured experimentally. The bottom emission could be reflected by metal or distributed Bragg reflector mirrors<sup>23</sup>.

Sub-1° beam divergence angle is presented in Fig. 3d, according to the far-field pattern captured by an infrared camera. In comparison, a commercial VCSEL has a typical divergence angle of 20° (ref. <sup>2</sup>) and the beam quality of an edge emitter is usually worse. The current TCSEL design has a radially polarized beam of unity topological charge, agreeing with the calculation shown in Fig. 2f. In contrast to the regular Gaussian beam, a vector beam could have a tighter focus spot<sup>24</sup>, but suffering a larger divergence angle (by a factor of two)<sup>25</sup>. Following the beam-tailoring capability of PCSELs<sup>26</sup> with similar divergence angles, it might be possible to convert the donut beam of TCSEL into a Gaussian-like beam by further lattice engineering. Importantly, such a narrow divergence of TCSEL, without collimating lenses, can reduce the system size, complexity and cost in systems such as three-dimensional sensing<sup>23</sup>.

Side-mode suppression ratio (SMSR) of 55 dB and linewidth of 0.03 nm (Fig. 3b, inset) is obtained with the minimal spectral resolution of the OSA (0.01 nm) at the output power below 1 W (similar high SMSR and low linewidth are also observed for the TCSEL under continuous-wave operations; Supplementary Fig. s12). As the output peak power exceeds 1 W, the laser linewidth rebroadens (Fig. 3c). Although linewidth rebroadening is a well-known phenomena in semiconductor lasers at high bias<sup>3</sup>, its cause has been ascribed to various mechanisms including side-mode interaction,

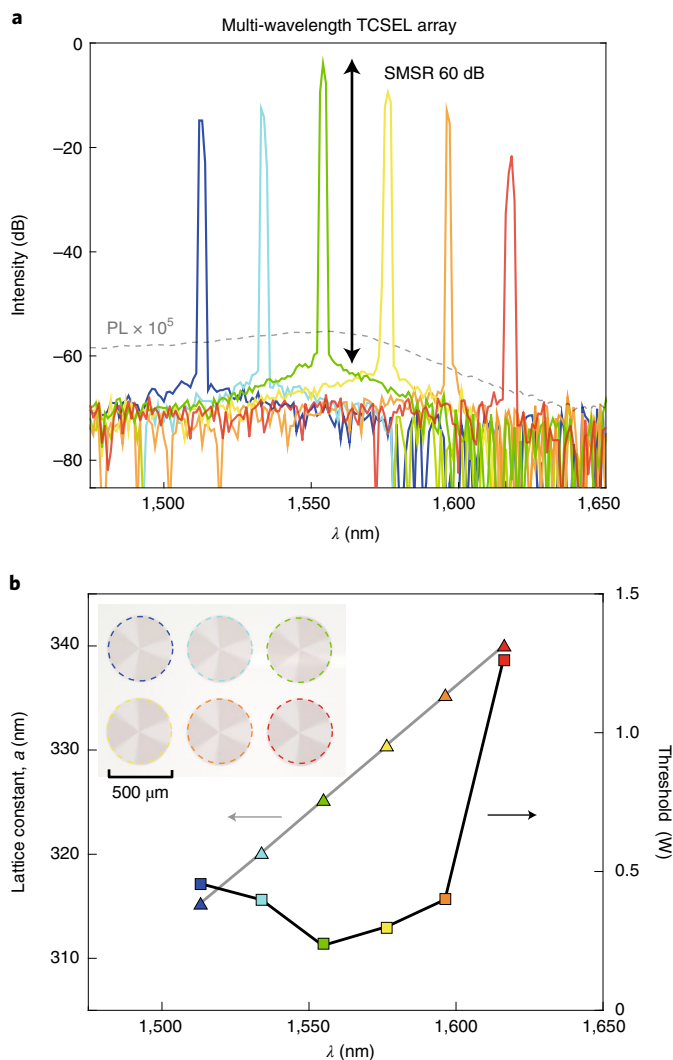


**Fig. 4 | Multi-wavelength 2D TCSEL array.** **a**, Lasing spectrum of a TCSEL with different lattice constants, taken using the OSA with 1 nm resolution. The dashed line represents the photoluminescence (PL) spectrum. **b**, Lasing thresholds and lasing wavelengths with different lattice constants. The inset shows the microscopy image of the TCSEL array.

spatial-hole burning, nonlinear gain and optical nonlinearity. Since there are no other modes except the topological lasing one in the  $\sim 4$  nm bandgap (Fig. 2c,d and Supplementary Fig. s13), rebroadening up to  $\sim 2$  nm is more likely due to nonlinearities rather than side modes. Nevertheless, such linewidth rebroadening can be alleviated by enlarging the cavity size or increasing the cavity loss (in the emission direction) as the cavity photon density (nonlinearity) reduces.

Surface-emitting lasers, compared with edge emitters, have the advantages of wafer-scale testing and monolithic 2D arrays. However, VCSEL lacks cost-effective solutions for long-wavelength operation as well as on-chip wavelength tunability<sup>2</sup>. Both limitations are tied to the fact that the vertical cavities are defined during epitaxial growth, which is highly material dependent and is uniform across the wafer. TCSEL has no such limitations because each planar cavity is lithographically defined.

A multi-wavelength TCSEL array is demonstrated in Fig. 4 by varying the lattice constant from 315 to 340 nm and the corresponding lasing wavelength scales linearly from 1,512 to 1,616 nm. Stable single-mode operations are observed for all the six lasers in the array; all of them have SMSR values larger

than 50 dB. The maximum SMSR value is 60 dB from the device with the lowest threshold, whose lasing wavelength is closest to the photoluminescence peak. The threshold rapidly increases for wavelengths higher than 1,600 nm, where the optical gain from the MQW is insufficient. Since the threshold rises much slower at shorter wavelengths, we expect the actual wavelength span of the TCSEL array to be larger than the 100 nm demonstrated here. The multi-wavelength TCSEL arrays can potentially enhance the wavelength-division multiplexing technology and multi-spectral sensing applications.

In conclusion, we introduce the TCSEL—a new surface-emitting laser having a much higher peak power and much narrower beam than conventional 1,550 nm single-mode semiconductor lasers. 1,550 nm is the wavelength with minimal fibre loss for global communications and the eye-safe wavelength for LiDAR in self-driving cars. A 2D TCSEL array is not only able to boost power but also vary wavelength—an intrinsic advantage over 1D wavelength-division-multiplexed DFB arrays and 2D mono-frequency VCSEL arrays. The route towards electrically injected TCSEL has been successfully paved by PCSEL diodes, and the topological nature of TCSEL may imply a larger and stabler single-mode device with better manufacturing yield. We believe that the TCSEL (array) has the potential to be an important laser source of future.

### Online content

Any methods, additional references, Nature Research reporting summaries, source data, extended data, supplementary information, acknowledgements, peer review information; details of author contributions and competing interests; and statements of data and code availability are available at <https://doi.org/10.1038/s41566-022-00972-6>.

Received: 15 September 2021; Accepted: 8 February 2022;  
Published online: 17 March 2022

### References

- Gao, X. et al. Dirac-vortex topological cavities. *Nat. Nanotechnol.* **15**, 1012–1018 (2020).
- Padullaparthi, B. D., Tatum, J. & Iga, K. *VCSEL Industry: Communication and Sensing* (John Wiley & Sons, 2021).
- Morthier, G. & Vankwikelberge, P. *Handbook of Distributed Feedback Laser Diodes* (Artech House, 2013).
- Hasan, M. Z. & Kane, C. L. Colloquium: topological insulators. *Rev. Mod. Phys.* **82**, 3045 (2010).
- Ozawa, T. et al. Topological photonics. *Rev. Mod. Phys.* **91**, 015006 (2019).
- Haus, H. & Shank, C. Antisymmetric taper of distributed feedback lasers. *IEEE J. Quantum Electron.* **12**, 532–539 (1976).
- Imada, M. et al. Coherent two-dimensional lasing action in surface-emitting laser with triangular-lattice photonic crystal structure. *Appl. Phys. Lett.* **75**, 316–318 (1999).
- Hirose, K. et al. Watt-class high-power, high-beam-quality photonic-crystal lasers. *Nat. Photon.* **8**, 406–411 (2014).
- Yoshida, M. et al. Double-lattice photonic-crystal resonators enabling high-brightness semiconductor lasers with symmetric narrow-divergence beams. *Nat. Mater.* **18**, 121–128 (2019).
- Hsu, M.-Y., Lin, G. & Pan, C.-H. Electrically injected 1.3- $\mu$ m quantum-dot photonic-crystal surface-emitting lasers. *Opt. Express* **25**, 32697–32704 (2017).
- Itoh, Y. et al. Continuous-wave lasing operation of 1.3- $\mu$ m wavelength InP-based photonic crystal surface-emitting lasers using MOVPE regrowth. *Opt. Express* **28**, 35483–35489 (2020).
- Hedlund, C. R. et al. Buried InP/airhole photonic-crystal surface-emitting lasers. *Phys. Status Solidi A* **218**, 2000416 (2021).
- Bian, Z. et al. 1.5  $\mu$ m epitaxially regrown photonic crystal surface emitting laser diode. *IEEE Photon. Technol. Lett.* **32**, 1531–1534 (2020).
- Bahari, B. et al. Nonreciprocal lasing in topological cavities of arbitrary geometries. *Science* **358**, 636–640 (2017).
- Bandres, M. A. et al. Topological insulator laser: experiments. *Science* **359**, eaar4005 (2018).
- Shao, Z.-K. et al. A high-performance topological bulk laser based on band-inversion-induced reflection. *Nat. Nanotechnol.* **15**, 67–72 (2020).

17. Zeng, Y. et al. Electrically pumped topological laser with valley edge modes. *Nature* **578**, 246–250 (2020).
  18. Dikopoltsev, A. et al. Topological insulator vertical-cavity laser array. *Science* **373**, 1514–1517 (2021).
  19. Ma, J. et al. Room-temperature continuous-wave Dirac-vortex topological lasers on silicon. Preprint at <https://arxiv.org/abs/2106.13838> (2021).
  20. Kogelnik, H. & Shank, C. V. Coupled-wave theory of distributed feedback lasers. *J. Appl. Phys.* **43**, 2327–2335 (1972).
  21. Liang, Y. et al. Three-dimensional coupled-wave analysis for triangular-lattice photonic-crystal surface-emitting lasers with transverse-electric polarization. *Opt. Express* **21**, 565–580 (2013).
  22. Lu, L. et al. Gain compression and thermal analysis of a sapphire-bonded photonic crystal microcavity laser. *IEEE Photon. Technol. Lett.* **21**, 1166–1168 (2009).
  23. Yoshida, M. et al. Photonic-crystal lasers with high-quality narrow-divergence symmetric beams and their application to LiDAR. *J. Phys. Photonics* **3**, 022006 (2021).
  24. Dorn, R., Quabis, S. & Leuchs, G. Sharper focus for a radially polarized light beam. *Phys. Rev. Lett.* **91**, 233901 (2003).
  25. Padgett, M. J., Miatto, F. M., Lavery, M. P. J., Zeilinger, A. & Boyd, R. W. Divergence of an orbital-angular-momentum-carrying beam upon propagation. *New J. Phys.* **17**, 023011 (2015).
  26. Miyai, E. et al. Lasers producing tailored beams. *Nature* **441**, 946–946 (2006).
- Publisher's note** Springer Nature remains neutral with regard to jurisdictional claims in published maps and institutional affiliations.
- © The Author(s), under exclusive licence to Springer Nature Limited 2022

## Methods

**Theoretical modelling.** A TCSEL consists of a large-area non-periodic structure, where non-uniformity is introduced by angular-dependent generalized Kekulé modulation of an otherwise periodic lattice. To efficiently model the resonances of the TCSEL, we adopt the coupled wave theory method<sup>21</sup> with spatial variation of in-plane and out-of-plane coupling coefficients. We consider the transverse-electric (TE) modes due to the TE QW gain.

For each honeycomb supercell (Fig. 2b), the in-plane field components  $E_{xy}$  can be expanded according to the Bloch's theorem. The coupling coefficients of the supercell are expressed via their Fourier components and they form a  $6 \times 6$  coupling matrix that contains coefficients of basic wave coupling, high-order wave coupling and radiation loss. Direct coupling represents the coupling of six basic waves with the lowest Fourier components, whereas the summation of all the other terms gives rise to the high-order coupling. We use 169 high-order waves in the simulation. The radiation loss is solved using the Green's function by assuming that the radiation coefficients are given by the diffraction of basic waves into the vertical direction.

Next, the whole cavity is discretized; on each node of the differential grid, the set of coupling matrices can be arranged according to the vortex phase and amplitude of the supercells. Based on the staggered-grid finite difference method, the resonance wavelengths and corresponding thresholds can be obtained by solving the complex eigenvalues of the coupling matrix. More details and results of our approach are being summarized into a separate paper.

**Device fabrication.** We use InGaAsP MQWs grown on an InP substrate as the gain material, which consists of four 10 nm wells sandwiched between 15 nm barriers. First, a 320 nm a-Si layer is deposited using the inductively coupled plasma (ICP)-enhanced chemical vapour deposition at the base chamber pressure of 1.5 Pa, temperature of 130 °C, radio-frequency (RF) power of 5 W and ICP power of 40 W. The gas flows are 15 s.c.c.m. for SiH<sub>4</sub>, 65 s.c.c.m. for H<sub>2</sub> and 250 s.c.c.m. for Ar. Spectroscopic ellipsometer (J.A. Woollam RC2) is used to measure the optical constants of the a-Si membrane in the wavelength range from 210 to 2,500 nm. As shown in Supplementary Fig. s7, the a-Si membrane is transparent for wavelengths above 1,000 nm, including both pump and lasing wavelengths.

The topological photonic crystals are patterned in the 320 nm a-Si layer by EBL and dry etching (ICP). Photoresist AR-P6200 is spin coated at 2,000 r.p.m. for 60 s and then baked on a hot plate at 150 °C for 60 s. Subsequently, the photoresist is exposed at 100 kV and 500 pA beam current with 200  $\mu\text{C cm}^{-2}$  dose using a JEOL JBX-6300FS EBL machine. The sample is developed using AR600-546 for 60 s and rinsed in AR600-60 for 30 s. Next, dry etching is performed using HBr with a flow of 50 s.c.c.m., ICP power of 750 W, RF power of 50 W at 20 °C and chamber pressure of 8 mTorr. The wafer is then cleaned in oxygen plasma (reactive ion etching) to remove the remnants of organic contamination and polymers at a

base pressure of 100 mTorr and temperature of 20 °C with O<sub>2</sub> gas at a flow rate of 50 s.c.c.m. and RF power of 100 W.

**Measurement setup.** As shown in Supplementary Fig. s8, the devices are optically pumped by a 1,064 nm fibre laser (SPI Instruments SP-100P-A-EP-Z-B-Y) with a 4 ns pulse width and repetition rate of 250 kHz. The pump beam illuminates the whole device after passing through a microscope objective lens (Mitutoyo 5X) with a long working distance and a numerical aperture of 0.14. The same objective lens is used to image the sample surface and collect the surface emission. The collected emission is then directed into a power meter (Thorlabs S146C), infrared camera (Hamamatsu C2741 infrared vidicon camera) and OSA (ANDO AQ6317). The time-domain waveforms of the pump and laser beams are monitored by an InGaAs detector (Thorlabs PDA015C/M).

## Data availability

All the relevant data are available from the corresponding author upon reasonable request.

## Acknowledgements

We thank C. Peng, M. H. Shih and Y. Liang for discussions and the Laboratory of Microfabrication, IOP CAS, for sample fabrication. This work was supported by the Chinese Academy of Sciences through the Project for Young Scientists in Basic Research (YSBR-021), the Strategic Priority Research Program (XDB33000000), the International Partnership Program with the Croucher Foundation (112111KY5B20200024), Beijing Natural Science Foundation (Z2000008), National Key R&D Program of China (2017YFA0303800) and Natural Science Foundation of China (12025409, 11721404 and 11974415).

## Author contributions

L.Y. fabricated and measured the devices. G.L. and X.G. performed the numerical simulations. L.L. led the project and wrote the manuscript with G.L.

## Competing interests

The authors declare no competing interests.

## Additional information

**Supplementary information** The online version contains supplementary material available at <https://doi.org/10.1038/s41566-022-00972-6>.

**Correspondence and requests for materials** should be addressed to Ling Lu.

**Peer review information** *Nature Photonics* thanks the anonymous reviewers for their contribution to the peer review of this work.

**Reprints and permissions information** is available at [www.nature.com/reprints](http://www.nature.com/reprints).